

Role of Matter Inhomogeneity on Fast Flavor Conversion of Supernova Neutrinos

Soumya Bhattacharyya^{1,*}, Meng-Ru Wu^{1,2,3,†} and Zewei Xiong^{4,‡}

¹*Institute of Physics, Academia Sinica, Taipei 115201, Taiwan*

²*Institute of Astronomy and Astrophysics, Academia Sinica, Taipei 106319, Taiwan*

³*Physics Division, National Center for Theoretical Sciences, Taipei 106319, Taiwan*

⁴*GSI Helmholtzzentrum für Schwerionenforschung, Planckstraße 1, D-64291 Darmstadt, Germany*

(Dated: April 16, 2025)

We investigated the impact of a spatially varying matter potential λ , coming from neutrino-electron forward scattering, on the emergence of fast neutrino flavor conversion (FFC) triggered by the presence of zero crossings in the angular distribution of the neutrino electron lepton number (ELN). We find that FFC can be significantly affected as the spatial variation rate of λ increases, and strong spatial variations can completely stabilize initially unstable systems. Using stability analysis based solely on initial conditions, we identified for the first time a critical variation rate above which no FFC occurs even if the flavor instability exists. By analyzing several representative matter profiles based on an $18 M_\odot$ SN model, we show that spatially inhomogeneous λ can suppress the occurrence of FFC associated with shallow ELN zero crossings in most of the SN's radial region, especially during the accretion phase. Our finding highlights the need to consider the impact of matter inhomogeneity in the development of improved SN models that aim to include the effect of neutrino flavor conversions.

Introduction.— Core-collapse supernovae (CCSNe) emit a vast number of neutrinos [1–5], whose self-interactions [6, 7] can drive fast flavor conversion (FFC) [8–10] at a rate proportional to the ambient neutrino number density and nearly 10^5 times faster than vacuum oscillations due to the presence of zero crossings in the angular distribution of the neutrino electron lepton number (ELN), shaped by the hierarchical interaction rates of intersecting ν_e and $\bar{\nu}_e$ fluxes [11–13]. Studies on local neutrino quantum kinetics ignoring spatial variation of the matter potential from neutrino-electron interactions show that FFCs cause flavor depolarization, erasing flavor differences in terms of ELN zero crossings in neutrino fluxes based on lepton asymmetry and angular modes [14–35] with significant implications for astrophysical and nucleosynthetic processes in CCSNe [28, 36–43]; see [44] for a recent review). Analyses of modern three-dimensional CCSN simulations revealed that FFC is more prominent in post-shock regions inside and above the proto-neutron star (PNS) within $O(0.1 - 1) s$ [45–52]. During this space-time domain, the overall magnitude and spatial variation rate of the matter potential are significant, often matching or exceeding that of the neutrino self-interaction potential [44, 53–55], thus necessitating further study on FFC that incorporates the spatially inhomogeneous matter potential in neutrino quantum kinetics [56].

In this *Letter*, we investigate for the first time how spatial inhomogeneity of the matter potential can significantly impact the emergence and evolution of FFC, depending on the strength of a dimensionless parameter γ , which roughly represents the ratio of the square of the neutrino self-interaction strength to the matter potential's spatial variation rate. With $\gamma < 1$, a system that is initially unstable for FFC without matter inhomogeneity can be fully stabilized by a strongly varying

matter potential, effectively suppressing FFC. We perform numerical simulations and a detailed local stability analysis [11, 57] to examine flavor growth dependence on γ and derive an analytical expression for the critical spatial variation rate of the matter potential, beyond which $\gamma < 1$ holds, based solely on the initial neutrino angular distribution. We apply this criteria to typical CCSN post-bounce matter profiles based on an $18 M_\odot$ SN simulation data to show that matter inhomogeneity at both pre- and post-shocked regions, particularly during the accretion phase, can suppress FFCs associated with shallow ELN zero crossings, of which the presence has been suggested by recent FFC studies without considering matter inhomogeneity [29, 30, 43, 58, 59]. Our finding highlights the importance of fully including this effect to understand the emergence and evolution of FFCs in a realistic SN environment.

Set-up & Notation.— To illustrate the phenomenon, we consider a dense, non-stationary, inhomogeneous, axially symmetric neutrino system within a small radial region Δz along the radial axis (denoted as z axis) inside a CCSN. Using the flavor-isospin convention [60, 61], neutrinos and antineutrinos are treated together, with antineutrinos represented as particles with negative energy and negative phase-space densities. Approximating the neutrino angular distribution by a simplified two-beam model [61] with radial velocities $v_+ = +1$ and $v_- = -1$, and neglecting vacuum oscillations, external forces, and momentum-changing collisions, the evolution for two neutrino flavors at any space-time point (z, t) within Δz is governed by the following equation of motion [7, 14]:

$$(\partial_t + \partial_z)\mathbf{S}_+ = (\boldsymbol{\lambda} - 2\mu\alpha\mathbf{S}_-) \times \mathbf{S}_+, \quad (1a)$$

$$(\partial_t - \partial_z)\mathbf{S}_- = (\boldsymbol{\lambda} + 2\mu\mathbf{S}_+) \times \mathbf{S}_-. \quad (1b)$$

In Eqs. (1a)-(1b), $\mathbf{S}_\pm[z, t]$ represents a three-dimensional flavor-space vector with basis $\{\hat{e}_1, \hat{e}_2, \hat{e}_3\}$, describing the flavor composition of neutrinos traveling at velocity $v_\pm = \pm 1$ at a specific space-time point (z, t) . Note that we will omit the explicit z, t dependence of quantities unless needed for emphasis, shown as [...], e.g., $\mathbf{S}_\pm[z, t]$. The longitudinal component along \hat{e}_3 is S_\pm^\parallel , while the transverse components in the $\hat{e}_1 - \hat{e}_2$ plane are represented by a two-dimensional vector \mathbf{S}_\pm^\perp , with $|\mathbf{S}_\pm^\perp| = \sqrt{1 - (S_\pm^\parallel)^2}$ that can be associated with the amount of flavor conversion. In Eqs. (1a)-(1b), $\lambda = \lambda(0, 0, 1)$, where $\lambda(z) = \sqrt{2}G_F n_e(z)$, represents the matter potential due to neutrino forward scattering with inhomogeneous background electrons of density n_e . Meanwhile, $\mu = \sqrt{2}G_F n_{\nu_e}$ characterizes the strength of the neutrino self-interaction potential originating from neutrino forward scattering among themselves. α is the initial neutrino number density ratio of the $v = -1$ to $v = +1$ mode, representing the depth of the zero crossing in the neutrino angular distribution for our two-beam model.

Without loss of generality, we set $\alpha = 1/3$, $\mu = 1.5 \text{ cm}^{-1}$, and let λ vary linearly in the z direction, defined by $\lambda = m(z + 30) \text{ cm}^{-1}$. Here, m represents the rate of spatial variation of λ along the z -direction. We take different values of $m = \{10^{-6}, 10^{-4}, 10^{-2}, 0.5, 1, 1.5, 2, 5, 10, 20\} \text{ cm}^{-2}$. Using the finite volume (FV) version of the COSE ν solver [62], Eqs. (1a)-(1b) are solved up to $t = 1.8 \text{ ns}$ with periodic boundary conditions¹ over $z \in \Delta z = (-30, +30) \text{ cm}$ discretized by 6,000 uniform grids, initializing $S_\pm^\parallel[z, t = 0] = \sqrt{1 - \mathbf{S}_x^2[z, t = 0]}$, $\mathbf{S}_x[z, t = 0] = 10^{-6} e^{-z^2/(2w^2)}$ and $\mathbf{S}_y[z, t = 0] = 0$, with $w = 5 \text{ cm}$.

Effect of matter inhomogeneity.— We define the measure of the overall FFC in the simulation domain Δz as $\mathcal{S}_\pm^{\text{trans}}$, given by

$$\mathcal{S}_\pm^{\text{trans}}[t] = \frac{1}{\Delta z} \int_{-\frac{\Delta z}{2}}^{\frac{\Delta z}{2}} dz \left| \mathbf{S}_\pm^\perp[z, t] \right|. \quad (2)$$

Its evolution in Fig. 1 reveals three regimes based on m :

- Small m ($0 \leq m [\text{cm}^2] \leq 10^{-2}$): $\mathcal{S}_\pm^{\text{trans}}$ behaves as in the absence of a matter term, leading to fast flavor depolarization. The flavor instability drives exponential growth of $\mathcal{S}_\pm^{\text{trans}}$ for $t \lesssim 0.6 \text{ ns}$ until it reaches $O(1)$ value.
- Intermediate m ($10^{-2} < m [\text{cm}^2] < 3$): The onset of FFC is delayed. For $m = 0.5$, growth starts

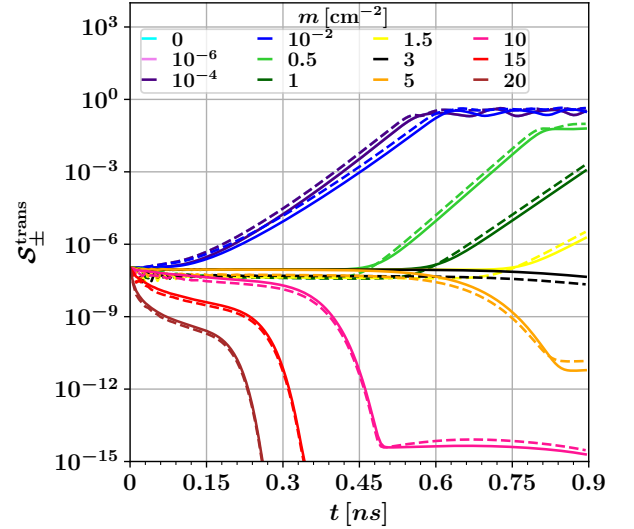


FIG. 1. Time evolution of $\mathcal{S}_\pm^{\text{trans}}[t]$ for spatially varying λ at different rates, denoted by m (ranging from 0 to 20 cm^{-2} as indicated in the legend) shown with different colors. Dashed and continuous lines represent $\mathcal{S}_+^{\text{trans}}[t]$ and $\mathcal{S}_-^{\text{trans}}[t]$, respectively. For $m = 0$, the simulation includes a constant matter term $\lambda = 3 \times 10^{-3} \text{ cm}^{-1}$. Lines with $m < 10^{-2} \text{ cm}^{-2}$ completely overlap with each other.

later ($t = 0.45 \text{ ns}$) and slower, reaching a reduced asymptotic value. Larger m values further delay and suppress instability growth.

- Large m ($m [\text{cm}^2] \geq 3$): $\mathcal{S}_\pm^{\text{trans}}$ decreases over time, with a faster decline for larger m , eventually stabilizing at a constant value that signifies no flavor conversion as $t \rightarrow \infty$.

Stability analysis: An analytical perspective.— To explain this new phenomena theoretically, we linearize Eqs. (1a)-(1b) introducing a new basis $Q_\pm[k, t]$, defined by,

$$Q_\pm[k, t] = \int dz e^{i(\lambda[z]t - kz)} (\mathbf{S}_\pm[z, t] \cdot (\hat{e}_1 - i\hat{e}_2)). \quad (3)$$

Eq. (3) reduces Eqs. (1a)-(1b) into a time-dependent ODE for each wavenumber k , removing explicit z -dependence while incorporating the spatial variation of $\lambda[z]$ through the constant slope m , resulting in the following form:

$$\partial_t \begin{pmatrix} Q_+ \\ Q_- \end{pmatrix} = \mathcal{A}_{2 \times 2}[t] \begin{pmatrix} Q_+ \\ Q_- \end{pmatrix}, \quad (4)$$

where

$$\mathcal{A}_{2 \times 2}[t] = \begin{pmatrix} -i(k - mt) + 2i\mu\alpha & -2i\mu\alpha \\ 2i\mu & i(k - mt) - 2i\mu \end{pmatrix}. \quad (5)$$

By performing a similarity transformation on Eq. (4) using a 2×2 matrix $P_{2 \times 2}[t]$, constructed from the eigenvectors of $\mathcal{A}_{2 \times 2}[t]$, to diagonalize $\mathcal{A}_{2 \times 2}[t]$ at each time

¹ As the form of λ introduces a discontinuity at the boundary, we only conduct our simulation up to the time when the flavor wave triggered by the central perturbation source of nonzero \mathbf{S}_x does not cross the boundary. We have verified that a different choice of Δz does not affect our result.

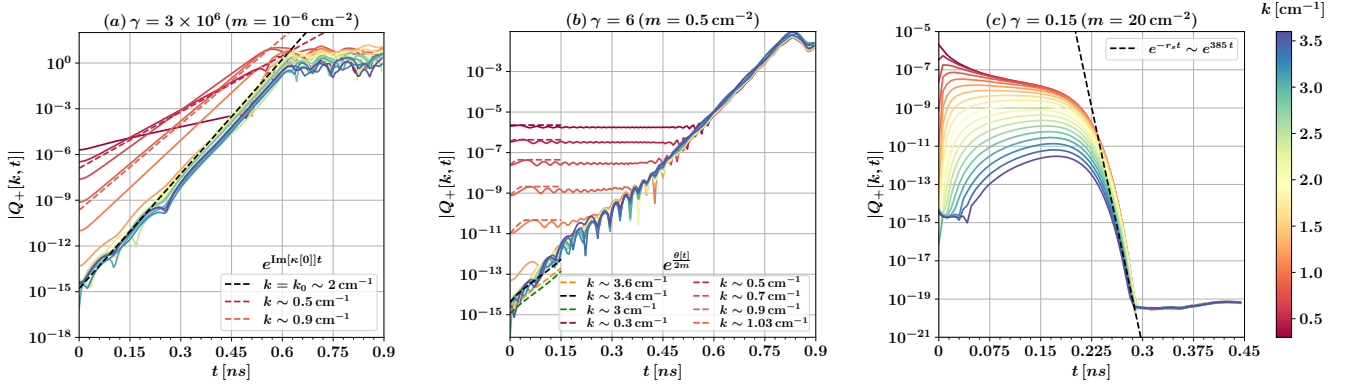


FIG. 2. Time evolution of $|Q_+[k, t]|$ for all initially unstable k modes ($k \in (0.3 - 3.6) \text{ cm}^{-1}$), shown as continuous lines with colors from the color bar. The left (a), middle (b), and right (c) panels correspond to small ($m = 10^{-6} \text{ cm}^{-2}$), intermediate ($m = 0.5 \text{ cm}^{-2}$), and large ($m = 20 \text{ cm}^{-2}$) m values, respectively. The dashed lines show analytical estimates as indicated in the legends of all three panels: $|Q_+[k, t]| \sim e^{\text{Im}[\kappa[0]]t}$ for $k = (0.5, 0.9, 2) \text{ cm}^{-1}$ in panel (a), $|Q_+[k, t]| \sim e^{\theta[t]/(2m)}$ for $k = (0.3, 0.5, 0.7, 0.9, 1.03, 3, 3.4, 3.6) \text{ cm}^{-1}$ in panel (b) within $t \sim (0 - 0.15) \text{ ns}$, and $|Q_+[k, t]| \sim e^{r_s t} \sim e^{-385t}$ for all k in panel (c) during its decline after $t \sim 0.15 \text{ ns}$.

for every Fourier mode k , the evolution of $Q_{\pm}[k, t]$ can be approximately given by

$$Q_{\pm}[k, t] \sim Q_{\pm}[k, 0] e^{-i\mu(1-\alpha)t - i \int_0^t \kappa[t] dt}, \quad (6)$$

where

$$\kappa[t] = \sqrt{(k - mt)^2 - 2(1 + \alpha)\mu(k - mt) + \mu^2(1 - \alpha)^2}. \quad (7)$$

The derivation of Eq. (6) from Eq. (4) assumes the existence of $P^{-1}[t]$ and that the elements of $P^{-1}[t] \frac{dP[t]}{dt}$ are much smaller than the eigenvalues of $\mathcal{A}_{2 \times 2}[t]$ (see Supplemental Materials (SM) for details). In our numerical setup, these conditions hold for all initial unstable k modes, but the applicable time range depends on m . For small m , they are valid from $t \sim 0 - 0.9 \text{ ns}$; for intermediate m , they hold from $0 \leq t \lesssim 0.15 \text{ ns}$; and for large m , from $t \sim 0.15 \text{ ns}$ onward (see SM). Eqs. (4)-(7) show that for $m \neq 0$, the evolution of $Q_{\pm}[k, t]$ follows a similar pattern as the $m = 0$ case, with k replaced by time-dependent $k_{\text{eff}}[t] = k - mt$, resulting in a time-dependent $\kappa[t]$, unlike the constant $\kappa[0]$ for $m = 0$ [61]. Importantly, $\kappa[t]$ retains the same functional form as $\kappa[0]$, with $k_{\text{eff}}[t]$ replacing k , and the evolution of $Q_{\pm}[k, t]$ is governed by the imaginary part of $\kappa[t]$, denoted by $\text{Im}[\kappa[t]]$.

In our two-beam model, $\text{Im}[\kappa[0]]$ is nonzero within $k \in (k_{\min}, k_{\max})$, where $k_{\min} = \mu(1 - \sqrt{\alpha})^2 \sim 0.3 \text{ cm}^{-1}$, $k_{\max} = \mu(1 + \sqrt{\alpha})^2 \sim 3.6 \text{ cm}^{-1}$. It reaches a maximum of $\beta = 2\mu\sqrt{\alpha} \sim 58 \text{ ns}^{-1}$ at $k = k_0 = \mu(1 + \alpha) \sim 2 \text{ cm}^{-1}$ and symmetrically decreases to zero on both sides of k_0 . Eq. (7) shows that replacing k with $k + mt$ leaves $\text{Im}[\kappa[t]]$ unchanged, meaning the value of $\text{Im}[\kappa[t]]$ at k for $t = 0$ shifts to $k + mt$ at time t . Thus, while the shape of $\text{Im}[\kappa[t]]$ in k space remains unchanged, the range of unstable k modes gradually shifts toward higher Fourier modes in the $k > 0$ (or $k < 0$) direction over time at a rate of

approximately $r_s \sim m/(k_{\max} - k_0) \sim 19(m/\text{cm}^{-2}) \text{ ns}^{-1}$. When $r_s \gtrsim \beta$, or equivalently, when the ratio $\gamma = \beta/r_s = 4\mu^2\alpha/m \lesssim 1$, the time evolution of $\text{Im}[\kappa[t]]$ becomes significant and the spatial variation of the matter potential starts influencing flavor growth due to the fast instability. The critical value of m can be determined solely from the initial ELN distribution using the relation $\gamma \sim 1$, which in our case is $m_{\text{crit}} \sim 3 \text{ cm}^{-2}$, in good agreement with the numerical solution shown in Fig. 1.

For small m ($\gamma \gg 1$), $\text{Im}[\kappa[t]]$ remains nearly time-independent, allowing $Q_{\pm}[k, t]$ for all initially unstable Fourier modes to grow independently at their initial rates ($\text{Im}[\kappa[0]]$), following $|Q_{\pm}[k, t]| \sim |Q_{\pm}[k, 0]| e^{\text{Im}[\kappa[0]]t}$ (see Eq. (6)), as if the matter potential were absent, until nonlinear effects induce fast flavor depolarization. Fig. 2(a) shows the numerical solution of Q_+ for $m = 10^{-6}$ ($\gamma \sim 3 \times 10^6$, $r_s = 19 \times 10^{-6} \text{ ns}^{-1} \ll \beta$), where all initially unstable k modes ($k \in (0.3, 3.6) \text{ cm}^{-1}$) exhibit independent exponential growth until saturating at $O(1)$ around $t \sim 0.6 \text{ ns}$. The analytical estimate of $\text{Im}[\kappa[0]]$ closely matches the numerical solution for $k \sim (0.5, 0.9, 2) \text{ cm}^{-1}$ [Fig. 2(a)], and the behavior of Q_+ also aligns with $\mathcal{S}_+^{\text{trans}}$ for small m (Fig. 1).

For intermediate m values ($1 \lesssim \gamma \lesssim O(100)$, $O(0.01\beta) \lesssim r_s \lesssim \beta$), some Fourier modes, especially those with higher initial growth rates (close to β) exhibit unstable growth with, however, different characteristics from the small m case. In our simulation with $m = 0.5 \text{ cm}^{-2}$, $\gamma \sim 6$ or $r_s \sim 10 \text{ ns}^{-1}$ [Fig. 2(b)], the linear evolution for $t < 0.15 \text{ ns}$ splits into stable modes ($k_{\min} \leq k < k_0$) and growing modes ($k_0 \leq k \leq k_{\max}$) with similar growth rates. Our analytical estimate of $|Q_+[k, t]|$ for $m = 0.5 \text{ cm}^{-2}$ given by Eq. (6) closely matches the numerical solution up to $t = 0.15 \text{ ns}$ for $k = \{0.3, 0.5, 0.7, 0.9, 1.03, 3, 3.4, 3.6\} \text{ cm}^{-1}$, as shown by the dashed lines in Fig. 2. The main driving factor be-

hind this behavior is the complex part of $\int_0^t \kappa[t] dt$, which for $m \neq 0$ can be simplified to:

$$\text{Im} \left[\int_0^t \kappa[t] dt \right] = \frac{(-k_{\text{eff}}[t] + \mu(1 + \alpha)) \text{Im}[\kappa[t]] + 4\alpha\mu^2 \theta[t]}{2m}, \quad (8)$$

where

$$\theta[t] = \begin{cases} \tan^{-1} \left(\frac{\text{Im}[\kappa[t]]}{k_{\text{eff}}[t] - \mu(1 + \alpha)} \right), & \text{if } k_{\text{eff}}[t] > \mu(1 + \alpha), \\ \tan^{-1} \left(\frac{\text{Im}[\kappa[t]]}{k_{\text{eff}}[t] - \mu(1 + \alpha)} \right) + \pi, & \text{if } k_{\text{eff}}[t] < \mu(1 + \alpha). \end{cases} \quad (9)$$

After $t = 0$ the first term on the right-hand side of Eq. (8) can be neglected compared to the more dominant $4\alpha\mu^2 \theta[t]$ to approximate $|Q_+[k, t]|$ as $|Q_+[k, 0]| \exp(4\alpha\mu^2 \theta[t]/2m)$, where the time-dependent rotation or change of $\theta[t]$ dictates the extent of flavor conversion (see SM). As t increases, $k_{\text{eff}} - \mu(1 + \alpha)$ becomes more negative for all k modes, while $\text{Im}[\kappa[t]]$ decreases due to the shift of instability map in k space but remains positive, driving $\theta[t]$ toward π regardless of k . In our numerical set-up considering $m = 0.5 \text{ cm}^{-2}$, $\theta[t]$ for $k < 2 \text{ cm}^{-1}$ modes starts just below π , requiring minimal change to reach π , leading to stability. In contrast, for $k > 2 \text{ cm}^{-1}$ modes, $\theta[t]$ starts much smaller than π , closer to 0, and undergoes a larger shift to approach π , during which instability develops. Over time, $\theta[t]$ flattens across k -space and tends toward a k -independent value near π , resulting in growth of $|Q_+[k, t]|$ with similar rates for modes with $k > 2 \text{ cm}^{-1}$. For $t > 0.15 \text{ ns}$, while $\theta[t]$ stabilizes near π , $|Q_+[k, t]|$ continues growing at the same rate for $k > 2 \text{ cm}^{-1}$ modes. Meanwhile, $|Q_+[k, t]|$ for previously stable $k < 2 \text{ cm}^{-1}$ modes begin to grow synchronously with the other modes until reaching nonlinearity at $t \sim 0.8 \text{ ns}$, significantly later than in the small m case, with each mode initiating growth only after neighboring modes reach similar magnitudes. This suggests interactions between stable and unstable modes, likely via a localized mode-mode coupling, requiring a collective Fourier mode treatment beyond $t = 0.15 \text{ ns}$, rather than independent evolution of Eq. (6) (see SM). The synchronization hints at coherent flavor structures, in contrast to the thermalized depolarization seen in the small m case, with potential implications on the asymptotic state of the system.

For large m values, Eqs. (6), and (8)-(9) predicts $|Q[k, t]| \sim \exp(\text{Im}[\kappa[t]]t)$, but with $\gamma < 1$, $\text{Im}[\kappa[t]]$ rapidly shifts in k space at a rate r_s exceeding β , causing it to quickly drop to zero over time for all initially unstable k modes, thus preventing their growth and suppressing significant flavor conversion. In our simulation with $m = 20 \text{ cm}^{-2}$ or $\gamma \sim 0.15$ [see Fig. 2(c)], $|Q[k, t]|$ for all initially unstable k -modes grow modestly at its initial growth rate over a short initial time period ($t \sim 0 - 0.15 \text{ ns}$). However, around $t \sim 0.15 \text{ ns}$, the rapid decrease of $\text{Im}[\kappa[t]]$ at rate r_s halts the growth and causes

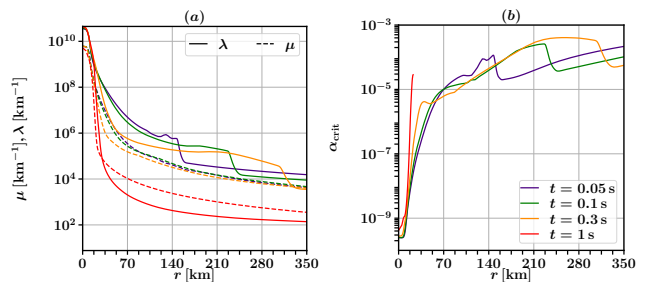


FIG. 3. Panel (a): Radial variation of μ (dashed) and λ (solid) from an $18 M_{\odot}$ SN model at four post-bounce phases: shock propagation ($t = 0.05 \text{ s}$), accretion ($t = 0.1 \text{ s}$, and 0.3 s), and Kelvin-Helmholtz cooling ($t = 1 \text{ s}$), shown by different colors. Panel (b): The corresponding critical ELN zero crossing depth parameter $\alpha_{\text{crit}} = m/(4\mu^2)$, derived from the local slope of λ .

$|Q[k, t]|$ for these modes to decay exponentially at a similar rate of $r_s \sim 385 \text{ ns}^{-1} \gg \beta$, as confirmed by the black dashed curve in Fig. 2(c). The exponential decay phase of $S_{\pm}^{\text{trans}}[t]$ for $m \geq 3 \text{ cm}^{-2}$ shown in Fig. 1 also supports this behavior. Within $O(10/r_s) \sim 0.1 \text{ ns}$, all initially unstable k modes stabilize, and $|Q[k, t]|$ remains constant, with $\text{Im}[\kappa[t]] \sim 0$ for all k , ensuring long-term stability when $mt/\mu \gg 1$. This demonstrates that a dense neutrino gas, initially susceptible to fast instabilities, can become stable under a strongly varying matter potential—an outcome independent of the simulation’s space-time domain.

A realistic SN scenario.— We apply the analysis of inhomogeneous matter effect to simulation data of an artificially exploded spherically-symmetric $18 M_{\odot}$ SN model from Ref. [63] at four snapshots: $t = 0.05 \text{ s}$ (initial shock propagation), $t = 0.1 \text{ s}$ and $t = 0.3 \text{ s}$ (early and later accretion phases), and $t = 1 \text{ s}$ (PNS cooling phase). For each snapshot, we compute $m(r) = d\lambda(r)/dr$ and $d\mu(r)/dr$ based on $\lambda(r)$ and $\mu(r)$ shown in Fig. 3(a). We apply our analytical criteria to the radial range where $d\lambda(r)/dr \gtrsim d\mu(r)/dr$, which is valid in $r \leq 350 \text{ km}$ for $t = 0.05 \text{ s}$, $t = 0.1 \text{ s}$, and $t = 0.3 \text{ s}$, as well as $r \lesssim 30 \text{ km}$ for $t = 1 \text{ s}$. Assuming that the fast instability growth rate originating from a possible ELN zero crossing can be approximated by the simple two-beam model discussed above, we can define $\alpha_{\text{crit}}(r) = m(r)/(4\mu^2(r))$, which represents the critical zero crossing depth parameter corresponding to $\gamma = 1$. Since the matter inhomogeneity effect can suppress FFC for $\alpha < \alpha_{\text{crit}}$, a larger α_{crit} indicates that the local ELN zero crossing needs to have a large depth for fast instability to develop.

Fig. 3(b) shows that $\alpha_{\text{crit}}(r)$ generally increases with radius in all snapshots. For $t = 0.05 \text{ s}$, $t = 0.1 \text{ s}$ and $t = 0.3 \text{ s}$, $10^{-5} \lesssim \alpha_{\text{crit}} \lesssim 10^{-3}$ in regions above the PNS. Since such α values are comparable to or larger than the shallow ELN zero crossing depths observed in post-shocked regions in simulations that implemented effect

of FFCs in neutrino transport [30, 43], this suggests that the matter inhomogeneity effect can influence the development and evolution of FFCs during the phase pertinent to shock revival. For $t = 1$ s, $\alpha_{\text{crit}} \lesssim 10^{-5}$ at regions where $d\lambda/dr \gtrsim d\mu/dr$.

Summary & Outlook.— We have performed a detailed analysis on how local matter inhomogeneity affects the development of FFCs. Assuming the spatial variation of matter potential λ , characterized by $m = d\lambda/dr$, is much larger than that of μ , we performed numerical simulations showing that matter inhomogeneity can delay or even completely suppress the onset of FFC when m exceeds a critical value. Our local stability analysis in the comoving frame of λ reveals that the effect of matter variation can be casted as introducing a time-dependent shift on the range of unstable Fourier modes in k space at a rate $r_s = 2m/\Delta k$, where Δk is the range of unstable Fourier modes without matter effect. The critical value of m can be determined by evaluating a dimensionless parameter $\gamma = \beta/r_s$, the ratio between the maximum instability growth rate β and r_s . When $\gamma \gg 1$, the system behaves as if no matter term exists, leading to independent mode growth and fast flavor depolarization. Intermediate $\gamma \sim O(10)$ results in delayed or suppressed FFCs with synchronized mode evolution. For $\gamma \ll 1$, large matter inhomogeneity completely suppress the flavor instability such that all Fourier modes decay as $e^{-r_s t}$. This analysis allows for quantitative determination of whether a given amount of spatial matter variation can affect the evolution of fast instability associated with the neutrino angular ELN zero crossings.

Based on our analytical criteria, we have further examined typical SN matter profiles and found that this matter inhomogeneity effect should be considered when shallow ELN crossings, quantified by the depth parameter α that reaches up to $\sim 10^{-3}$, are present, particularly during the accretion phase critical for shock revival. As recent studies found that angular crossings in the neutrino spectrum should evolve from no ELN angular crossings to at most shallow crossings that have weak instabilities, corresponding to a transition from small to intermediate γ values, this suggests that the evolution of FFCs in a realistic environment can be substantially affected by matter inhomogeneity effect. In particular, the synchronized evolution of different Fourier modes observed for $\gamma \sim O(10 - 100)$ indicates that the flavor evolution and its nonlinear state for weak crossing cases can be very different from those obtained without considering matter inhomogeneity, which requires further studies.

While we focused on FFCs from a simple model with two velocity modes in this work, the conclusion should be applicable to cases with continuous angular distributions. Moreover, we expect a similar or even stronger impact of matter inhomogeneity on slow and collisional instabilities due to their intrinsically weaker unstable growth rates [44, 64, 65], warranting further explorations. In the

same spirit, potential impact due to temporal variation of λ may also be relevant. All these should be addressed to fully understand the role of neutrinos and their flavor oscillations in SN as well as in binary neutron star mergers, highlighting the profound implication of our work in this working direction.

Acknowledgments.— We thank Sajad Abbar, Heng-Hao Chen, Huaiyu Duan, and Manu George for insightful discussions on the set-up and the results of this work. S. B. and M.R.W. acknowledge support of the National Science and Technology Council, Taiwan under Grant No. 111-2628-M-001-003-MY4, and the Academia Sinica (Project Nos. AS-CDA-109-M11 and AS-IV-114-M04). M.R.W. also acknowledges support from the Physics Division of the National Center for Theoretical Sciences, Taiwan. Z.X. acknowledges support of the European Research Council (ERC) under the European Union’s Horizon 2020 research and innovation program (ERC Advanced Grant KILONOVA No. 885281) and under the ERC Starting Grant (NeuTrAE, No. 101165138).

The work is partially funded by the European Union. Views and opinions expressed are however those of the author(s) only and do not necessarily reflect those of the European Union or the European Research Council Executive Agency. Neither the European Union nor the granting authority can be held responsible for them.

* soumyabhattacharyya475@gmail.com

† mwu@as.edu.tw

‡ z.xiong@gsi.de

- [1] A. Mirizzi, I. Tamborra, H.-T. Janka, N. Saviano, K. Scholberg, R. Bollig, L. Hüdepohl, and S. Chakraborty, *Nuovo Cimento Rivista Serie* **39**, 1 (2016), [arXiv:1508.00785](https://arxiv.org/abs/1508.00785) [astro-ph.HE].
- [2] A. Burrows and D. Vartanyan, *Nature* **589**, 29 (2021), [arXiv:2009.14157](https://arxiv.org/abs/2009.14157) [astro-ph.SR].
- [3] A. Mezzacappa, E. Endeve, O. E. Bronson Messer, and S. W. Bruenn, *Liv. Rev. Comput. Astrophys.* **6**, 4 (2020), [arXiv:2010.09013](https://arxiv.org/abs/2010.09013) [astro-ph.HE].
- [4] T. Fischer, G. Guo, K. Langanke, G. Martinez-Pinedo, Y.-Z. Qian, and M.-R. Wu, *Prog. Part. Nucl. Phys.* **137**, 104107 (2024), [arXiv:2308.03962](https://arxiv.org/abs/2308.03962) [astro-ph.HE].
- [5] H. T. Janka, (2025), [arXiv:2502.14836](https://arxiv.org/abs/2502.14836) [astro-ph.HE].
- [6] J. T. Pantaleone, *Phys. Lett. B* **287**, 128 (1992).
- [7] G. Sigl and G. Raffelt, *Nuclear Physics B* **406**, 423 (1993).
- [8] R. F. Sawyer, *Phys. Rev. D* **72**, 045003 (2005), [arXiv:hep-ph/0503013](https://arxiv.org/abs/hep-ph/0503013) [astro-ph].
- [9] R. F. Sawyer, *Phys. Rev. D* **79**, 105003 (2009), [arXiv:0803.4319](https://arxiv.org/abs/0803.4319).
- [10] R. F. Sawyer, *Phys. Rev. Lett.* **116**, 081101 (2016), [arXiv:1509.03323](https://arxiv.org/abs/1509.03323).
- [11] I. Izaguirre, G. Raffelt, and I. Tamborra, *Phys. Rev. Lett.* **118**, 021101 (2017), [arXiv:1610.01612](https://arxiv.org/abs/1610.01612) [hep-ph].
- [12] T. Morinaga, *Phys. Rev. D* **105**, L101301 (2022), [arXiv:2103.15267](https://arxiv.org/abs/2103.15267).
- [13] B. Dasgupta, *Phys. Rev. Lett.* **128**, 081102 (2022),

- arXiv:2110.00192.
- [14] S. Bhattacharyya and B. Dasgupta, *Phys. Rev. Lett.* **126**, 061302 (2021), arXiv:2009.03337 [hep-ph].
- [15] S. Bhattacharyya and B. Dasgupta, *Phys. Rev. D* **102**, 063018 (2020), arXiv:2005.00459.
- [16] M.-R. Wu, M. George, C.-Y. Lin, and Z. Xiong, *Phys. Rev. D* **104**, 103003 (2021), arXiv:2108.09886 [hep-ph].
- [17] S. Richers, D. E. Willcox, N. M. Ford, and A. Myers, *Phys. Rev. D* **103**, 083013 (2021), arXiv:2101.02745.
- [18] S. Richers, D. Willcox, and N. Ford, *Phys. Rev. D* **104**, 103023 (2021), arXiv:2109.08631.
- [19] S. Richers, H. Duan, M.-R. Wu, S. Bhattacharyya, M. Zaizen, M. George, C.-Y. Lin, and Z. Xiong, *Phys. Rev. D* **106**, 043011 (2022), arXiv:2205.06282.
- [20] S. Bhattacharyya and B. Dasgupta, *Phys. Rev. D* **106**, 103039 (2022), arXiv:2205.05129.
- [21] M. Zaizen and H. Nagakura, *Phys. Rev. D* **107**, 103022 (2023), arXiv:2211.09343 [astro-ph.HE].
- [22] M. Zaizen and H. Nagakura, *Phys. Rev. D* **107**, 123021 (2023), arXiv:2304.05044 [astro-ph.HE].
- [23] Z. Xiong, M.-R. Wu, S. Abbar, S. Bhattacharyya, M. George, and C.-Y. Lin, *Phys. Rev. D* **108**, 063003 (2023).
- [24] H. Nagakura, L. Johns, and M. Zaizen, *Phys. Rev. D* **109**, 083013 (2024), arXiv:2312.16285 [astro-ph.HE].
- [25] H. Nagakura and M. Zaizen, *Phys. Rev. D* **108**, 123003 (2023), arXiv:2308.14800 [astro-ph.HE].
- [26] M. Cornelius, S. Shalgar, and I. Tamborra, *JCAP* **02**, 038 (2024), arXiv:2312.03839 [astro-ph.HE].
- [27] M. Delfan Azari, H. Sasaki, T. Takiwaki, and H. Okawa, *PTEP* **2024**, 103E01 (2024), arXiv:2402.04741 [hep-ph].
- [28] Z. Xiong, M.-R. Wu, M. George, C.-Y. Lin, N. Khosravi Largani, T. Fischer, and G. Martínez-Pinedo, *Phys. Rev. D* **109**, 123008 (2024), 2402.19252.
- [29] D. F. G. Fiorillo and G. G. Raffelt, *Phys. Rev. Lett.* **133**, 221004 (2024), arXiv:2403.12189 [hep-ph].
- [30] Z. Xiong, M.-R. Wu, M. George, and C.-Y. Lin, *Phys. Rev. Lett.* **134**, 051003 (2025), arXiv:2403.17269 [astro-ph.HE].
- [31] S. Shalgar and I. Tamborra, *JCAP* **09**, 021 (2024), arXiv:2406.09504 [astro-ph.HE].
- [32] S. Richers, J. Froustey, S. Ghosh, F. Foucart, and J. Gomez, *Phys. Rev. D* **110**, 103019 (2024), arXiv:2409.04405 [astro-ph.HE].
- [33] M. George, Z. Xiong, M.-R. Wu, and C.-Y. Lin, *Phys. Rev. D* **110**, 123018 (2024), arXiv:2409.08833 [astro-ph.HE].
- [34] D. F. G. Fiorillo and G. G. Raffelt, (2025), arXiv:2502.06935 [hep-ph].
- [35] J. Liu, H. Nagakura, M. Zaizen, L. Johns, and S. Yamada, (2025), arXiv:2503.18145 [astro-ph.HE].
- [36] Z. Xiong, A. Sieverding, M. Sen, and Y.-Z. Qian, *Astrophys. J.* **900**, 144 (2020), arXiv:2006.11414 [astro-ph.HE].
- [37] S.-I. Fujimoto and H. Nagakura, *Mon. Not. R. Astron. Soc.* **519**, 2623 (2023), arXiv:2210.02106.
- [38] J. Ehring, S. Abbar, H. T. Janka, G. Raffelt, and I. Tamborra, *Phys. Rev. D* **107**, 103034 (2023), arXiv:2301.11938.
- [39] J. Ehring, S. Abbar, H. T. Janka, G. Raffelt, and I. Tamborra, *Phys. Rev. Lett.* **131**, 061401 (2023), arXiv:2305.11207.
- [40] H. Nagakura, *Phys. Rev. Lett.* **130**, 211401 (2023), arXiv:2301.10785 [astro-ph.HE].
- [41] H. Nagakura and K. Sumiyoshi, (2024), arXiv:2401.15180.
- [42] K. Mori, T. Takiwaki, K. Kotake, and S. Horiuchi, (2025), arXiv:2501.15256 [astro-ph.HE].
- [43] T. Wang and A. Burrows, (2025), arXiv:2503.04896 [astro-ph.HE].
- [44] L. Johns, S. Richers, and M.-R. Wu, (2025), 10.1146/annurev-nucl-121423-100853, arXiv:2503.05959 [astro-ph.HE].
- [45] S. Abbar, H. Duan, K. Sumiyoshi, T. Takiwaki, and M. C. Volpe, *Phys. Rev. D* **100**, 043004 (2019), arXiv:1812.06883 [astro-ph.HE].
- [46] M. Delfan Azari, S. Yamada, T. Morinaga, W. Iwakami, H. Okawa, H. Nagakura, and K. Sumiyoshi, *Phys. Rev. D* **99**, 103011 (2019), arXiv:1902.07467.
- [47] R. Glas, H.-T. Janka, F. Capozzi, M. Sen, B. Dasgupta, A. Mirizzi, and G. Sigl, *Phys. Rev. D* **101**, 063001 (2020), arXiv:1912.00274.
- [48] T. Morinaga, H. Nagakura, C. Kato, and S. Yamada, *Phys. Rev. Res.* **2**, 012046(R) (2020), arXiv:1909.13131 [astro-ph.HE].
- [49] F. Capozzi, S. Abbar, R. Bollig, and H. T. Janka, *Phys. Rev. D* **103**, 063013 (2021), arXiv:2012.08525 [astro-ph.HE].
- [50] S. Abbar, F. Capozzi, R. Glas, H. T. Janka, and I. Tamborra, *Phys. Rev. D* **103**, 063033 (2021), arXiv:2012.06594.
- [51] H. Nagakura, A. Burrows, L. Johns, and G. M. Fuller, *Phys. Rev. D* **104**, 083025 (2021), arXiv:2108.07281 [astro-ph.HE].
- [52] R. Akaho, J. Liu, H. Nagakura, M. Zaizen, and S. Yamada, **109**, 023012 (2024), arXiv:2311.11272.
- [53] S. Chakraborty, T. Fischer, A. Mirizzi, N. Saviano, and R. Tomàs, *Phys. Rev. Lett.* **107**, 151101 (2011), arXiv:1104.4031.
- [54] S. Chakraborty, R. S. Hansen, I. Izaguirre, and G. G. Raffelt, *J. Cosmol. Astropart. Phys.* **2016**, 28 (2016), arXiv:1507.07569.
- [55] Z. Xiong, M.-R. Wu, G. Martínez-Pinedo, T. Fischer, M. George, C.-Y. Lin, and L. Johns, *Phys. Rev. D* **107**, 083016 (2023), arXiv:2210.08254 [astro-ph.HE].
- [56] G. Sigl, *Phys. Rev. D* **105**, 043005 (2022), arXiv:2109.00091.
- [57] A. Banerjee, A. Dighe, and G. Raffelt, *Phys. Rev. D* **84**, 053013 (2011), arXiv:1107.2308.
- [58] L. Johns, (2024), arXiv:2401.15247 [astro-ph.HE].
- [59] J. Liu, H. Nagakura, M. Zaizen, L. Johns, R. Akaho, and S. Yamada, *Phys. Rev. D* **111**, 023051 (2025), arXiv:2411.08503 [astro-ph.HE].
- [60] H. Duan, G. M. Fuller, and Y.-Z. Qian, *Phys. Rev. D* **74**, 123004 (2006), arXiv:0703776 [astro-ph].
- [61] S. Chakraborty, R. S. Hansen, I. Izaguirre, and G. G. Raffelt, *J. Cosmol. Astropart. Phys.* **2016**, 42 (2016), arXiv:1602.00698.
- [62] M. George, C.-Y. Lin, M.-R. Wu, T. G. Liu, and Z. Xiong, *Comput. Phys. Commun.* **283**, 108588 (2023), arXiv:2203.12866.
- [63] T. Fischer, S. C. Whitehouse, A. Mezzacappa, F.-K. K. Thielemann, and M. Liebendörfer, *Astron. Astrophys.* **517**, A80 (2010), arXiv:0908.1871.
- [64] H. Duan, G. M. Fuller, and Y.-Z. Qian, *Annu. Rev. Nucl. Part.* **60**, 569 (2010), arXiv:1001.2799 [hep-ph].
- [65] L. Johns, *Phys. Rev. Lett.* **130**, 191001 (2023), arXiv:2104.11369.

- [66] S. Abbar, *Phys. Rev. D* **103**, 045014 (2021),
[arXiv:2007.13655 \[astro-ph.HE\]](#).

Supplemental Material to “Role of Matter Inhomogeneity on Fast Flavor Conversion of Supernova Neutrinos”

Soumya Bhattacharyya, Meng-Ru Wu and Zewei Xiong

In this supplemental material, we provide a detailed explanation of the stability analysis theory outlined in the main text to examine how the spatial variation rate of the matter potential influences the initial growth of flavor instability in the system. In this context, we also present a comprehensive derivation of Eq. (6) in the main text.

Stability analysis Theory

In this section, we introduce our new stability analysis framework, incorporating the effects of the inhomogeneous matter potential. To achieve this, we begin by linearizing Eqs. (1a)-(1b) in the main text under the approximation $S_{\pm}^{\parallel}[z, t] = 1$, resulting in the following matrix equation expressed in terms of $S_{\pm}^{\perp}[z, t] = \mathbf{S}_{\pm}[z, t] \cdot (\hat{\mathbf{e}}_1 - i\hat{\mathbf{e}}_2)$:

$$i \begin{pmatrix} \partial_t + \partial_z & 0 \\ 0 & \partial_t - \partial_z \end{pmatrix} \begin{pmatrix} S_{+}^{\perp} \\ S_{-}^{\perp} \end{pmatrix} = \begin{pmatrix} \lambda[z] - 2\mu\alpha & 2\mu\alpha \\ -2\mu & \lambda[z] + 2\mu \end{pmatrix} \begin{pmatrix} S_{+}^{\perp} \\ S_{-}^{\perp} \end{pmatrix}. \quad (\text{S1})$$

We define a new basis, $Q_{\pm}[k, t]$, using the following relation:

$$S_{\pm}^{\perp}[z, t] = \int_{-\infty}^{\infty} dk e^{i(kz - \lambda[z]t)} Q_{\pm}[k, t], \quad (\text{S2})$$

where $\lambda[z] = m(z + 30)$. It is important to note that Eq. (S2) represents the Fourier transform of $S_{\pm}^{\perp}[z, t]$ in the comoving frame of $\lambda[z]$. Substituting Eq. (S2) into Eq. (S1), we can write the time evolution of $Q_{\pm}[k, t]$ for each k mode in terms of the following ordinary differential equation of matrix form:

$$\partial_t \begin{pmatrix} Q_{+} \\ Q_{-} \end{pmatrix} = \mathcal{A}_{2 \times 2}[t] \begin{pmatrix} Q_{+} \\ Q_{-} \end{pmatrix}, \quad (\text{S3})$$

where

$$\mathcal{A}_{2 \times 2}[t] = \begin{pmatrix} -i(k - mt) + 2i\mu\alpha & -2i\mu\alpha \\ 2i\mu & i(k - mt) - 2i\mu \end{pmatrix}. \quad (\text{S4})$$

The $e^{-i\lambda[z]t}$ term in the basis transformation of Eq. (S2) plays a key role in canceling the z dependent $\lambda[z]$ term from the right-hand side of Eq. (S1). When the Liouville operator on the left-hand side acts on this term, it produces $(\partial_t \pm \partial_z)e^{-i\lambda[z]t} = -i(\lambda[z] \pm \frac{d\lambda[z]}{dz}t)e^{-i\lambda[z]t}$. The first term cancels the z dependent $\lambda[z]$ term on the right-hand side, leaving only the $\frac{d\lambda[z]}{dz}t$ term. For $\lambda[z]$ varying linearly in z with slope m , this simplifies to mt , removing the explicit z -dependence in the equation of motion for Q_{\pm} . This step is crucial as it allows us to analyze the time evolution of $Q_{\pm}[k, t]$ for each Fourier mode k independently using Eq. (S3). To solve Eq. (S3), we introduce a new basis $(\tilde{Q}_{+}[k, t], \tilde{Q}_{-}[k, t])$, which is connected to the original basis $(Q_{+}[k, t], Q_{-}[k, t])$ through the following relation:

$$\begin{pmatrix} Q_{+}[k, t] \\ Q_{-}[k, t] \end{pmatrix} = P_{2 \times 2}[t] \begin{pmatrix} \tilde{Q}_{+}[k, t] \\ \tilde{Q}_{-}[k, t] \end{pmatrix} = (T_{X_1}[t], T_{X_2}[t])_{2 \times 2} \begin{pmatrix} \tilde{Q}_{+}[k, t] \\ \tilde{Q}_{-}[k, t] \end{pmatrix}. \quad (\text{S5})$$

In Eq. (S5), $T_{X_1}[t]$ and $T_{X_2}[t]$ are the 2×1 dimensional eigenvectors of the matrix $\mathcal{A}_{2 \times 2}[t]$ at time t corresponding to the eigenvalues $X_1[t]$ and $X_2[t]$, respectively. From this point forward, we will omit the subscript 2×2 when referring to 2×2 matrices.

From Eq. (S4), the characteristic equation of the matrix $\mathcal{A}[t]$ can be solved to determine the explicit expressions for the eigenvalues $(X_{1,2}[t])$ and eigenvectors $(T_{X_{1,2}}[t])$ as functions of time t , as shown below:

$$X_1[t] = \mu(1 - \alpha) + \kappa[t], \quad (\text{S6a})$$

$$X_2[t] = \mu(1 - \alpha) - \kappa[t], \quad (\text{S6b})$$

and

$$T_{X_1}[t] = \frac{1}{N_1[t]} \left(\frac{-2\mu\alpha}{k_{\text{eff}}[t] - 2\mu\alpha - X_1[t]} \right), \quad (\text{S7a})$$

$$T_{X_2}[t] = \frac{1}{N_2[t]} \left(\frac{-2\mu\alpha}{k_{\text{eff}}[t] - 2\mu\alpha - X_2[t]} \right). \quad (\text{S7b})$$

In Eqs. (S6a)-(S7b), $\kappa[t]$ and $k_{\text{eff}}[t]$ are defined as,

$$\kappa[t] = \sqrt{k_{\text{eff}}^2[t] - 2(1 + \alpha)\mu k_{\text{eff}}[t] + \mu^2(1 - \alpha)^2}, \quad (\text{S8a})$$

$$k_{\text{eff}}[t] = k - mt, \quad (\text{S8b})$$

$$N_1[t] = \sqrt{\left| \frac{2\mu\alpha}{k_{\text{eff}}[t] - 2\mu\alpha - X_1[t]} \right|^2 + 1}, \quad (\text{S8c})$$

$$N_2[t] = \sqrt{\left| \frac{2\mu\alpha}{k_{\text{eff}}[t] - 2\mu\alpha - X_2[t]} \right|^2 + 1}. \quad (\text{S8d})$$

In Eq. (S3), the dependence of k in $\mathcal{A}[t]$ is expressed as $k_{\text{eff}}[t] = k - mt$. Therefore, in the solution for $Q_{\pm}[k, t]$ (or $\tilde{Q}_{\pm}[k, t]$), k appears as $k_{\text{eff}}[t] = k - mt$. From now on, we will simplify the notation by writing $Q_{\pm}[t]$ instead of $Q_{\pm}[k, t]$ (and $\tilde{Q}_{\pm}[t]$ instead of $\tilde{Q}_{\pm}[k, t]$), omitting the explicit dependence on k and sometimes the time dependence when it is clear from context, particularly in differential equations. Moreover, the absolute value of $Q_{\pm}[t]$ will be represented as $|Q_{\pm}[t]|$. By applying the relation in Eq. (S5) and assuming the existence of $P^{-1}[t]$, the equation of motion for $\tilde{Q}_{\pm}[k, t]$ can be expressed as:

$$\partial_t \begin{pmatrix} \tilde{Q}_+ \\ \tilde{Q}_- \end{pmatrix} = \left(-i \begin{pmatrix} X_1[t] & 0 \\ 0 & X_2[t] \end{pmatrix} - P^{-1}[t] \frac{dP[t]}{dt} \right) \begin{pmatrix} \tilde{Q}_+ \\ \tilde{Q}_- \end{pmatrix}. \quad (\text{S9})$$

In Eq. (S9), $\frac{dP[t]}{dt}$ and $P^{-1}[t]$ matrices are defined by,

$$\frac{dP[t]}{dt} = \frac{1}{\kappa[t]} \begin{pmatrix} \frac{2m\alpha\mu(\delta_{\text{Im}[\kappa[t]],0} + N_1[t]^2(1 - \delta_{\text{Im}[\kappa[t]],0}))}{(N_1[t])^3(k_{\text{eff}}[t] - 2\mu\alpha - X_1[t])} & \frac{-2m\alpha\mu(\delta_{\text{Im}[\kappa[t]],0} + N_2[t]^2(1 - \delta_{\text{Im}[\kappa[t]],0}))}{(N_2[t])^3(k_{\text{eff}}[t] - 2\mu\alpha - X_2[t])} \\ \frac{4m\alpha^2\mu^2\delta_{\text{Im}[\kappa[t]],0}}{(N_1[t])^3(k_{\text{eff}}[t] - 2\mu\alpha - X_1[t])^2} & \frac{-4m\alpha^2\mu^2\delta_{\text{Im}[\kappa[t]],0}}{(N_2[t])^3(k_{\text{eff}}[t] - 2\mu\alpha - X_2[t])^2} \end{pmatrix}, \quad (\text{S10a})$$

$$P^{-1}[t] = \frac{1}{\det[P[t]]} \begin{pmatrix} \frac{1}{N_2[t]} & \frac{2\mu\alpha}{N_2[t](k_{\text{eff}}[t] - 2\mu\alpha - X_2[t])} \\ -\frac{1}{N_1[t]} & \frac{-2\mu\alpha}{N_1[t](k_{\text{eff}}[t] - 2\mu\alpha - X_1[t])} \end{pmatrix}, \quad (\text{S10b})$$

where $\det[P[t]]$ is the determinant of the matrix $P[t]$ and $\delta_{\text{Im}[\kappa[t]],0}$ is the Kronecker delta function, defined as follows:

$$\det[P[t]] = -\frac{\kappa[t]}{\mu N_1[t] N_2[t]}, \quad (\text{S11a})$$

$$\delta_{\text{Im}[\kappa[t]],0} = \begin{cases} 1, & \text{if } \text{Im}[\kappa[t]] = 0, \\ 0, & \text{if } \text{Im}[\kappa[t]] \neq 0. \end{cases} \quad (\text{S11b})$$

If the elements of $P^{-1}[t] \frac{dP[t]}{dt}$ are negligible compared to $X_{1,2}[t]$, an approximate solution for \tilde{Q}_{\pm} can be derived from Eq. (S9) as,

$$\tilde{Q}_+[t] = \tilde{Q}_+[0] e^{-i\mu(1-\alpha)t - i \int_0^t \kappa[t] dt}, \quad (\text{S12a})$$

$$\tilde{Q}_-[t] = \tilde{Q}_-[0] e^{-i\mu(1-\alpha)t + i \int_0^t \kappa[t] dt}. \quad (\text{S12b})$$

By utilizing Eqs. (S12a)-(S12b) along with the transformation formula from Eq. (S5), one can obtain the solution for $Q_{\pm}[t]$ as a function of time t for any given k mode. Eqs. (S12a)-(S12b) indicate that since μ and α are real, $\tilde{Q}_+[t]$

for a specific choice of k mode can exhibit exponential growth over time, leading to fast flavor instability, only if $\kappa[t]$ for those k modes becomes complex. In this case, $\tilde{Q}_-[t]$ corresponds to the exponentially decaying solution and therefore does not contribute to the growth of flavor instability, allowing us to approximate $\tilde{Q}_-[t] \sim 0$. Conversely, $\tilde{Q}_+[t]$ represents the exponentially growing solution. Furthermore, by applying the transformation in Eq. (S5), the solution for $Q_\pm[t]$ for k modes that exhibit exponential growth and drive fast flavor instability can be simplified as follows:

$$Q_+[t] \sim Q_+[0] \left(\frac{N_1[0]}{N_1[t]} \right) \left(\frac{N_{\text{eff}}[0]}{N_{\text{eff}}[t]} \right) e^{-i\mu(1-\alpha)t - i \int_0^t \kappa[t] dt}, \quad (\text{S13a})$$

$$Q_-[t] \sim Q_-[0] \left(\frac{N_1[0]}{N_1[t]} \right) e^{-i\mu(1-\alpha)t - i \int_0^t \kappa[t] dt}, \quad (\text{S13b})$$

where $N_{\text{eff}}[t]$ is defined as:

$$N_{\text{eff}}[t] = k_{\text{eff}}[t] - 2\mu\alpha - X_1[t]. \quad (\text{S14})$$

Eqs. (S13a)-(S13b) show that for $m \neq 0$, the evolution of $Q_\pm[t]$ resembles the $m = 0$ case, except that the wavenumber k is replaced by a time-dependent $k_{\text{eff}}[t] = k - mt$. This leads to time-dependent amplitude modulation proportional to $\frac{N_1[0]}{N_1[t]} \left(\frac{N_{\text{eff}}[0]}{N_{\text{eff}}[t]} \right)$ for $Q_+[t]$ (or $\frac{N_1[0]}{N_1[t]}$ for $Q_-[t]$) and a time-dependent frequency or growth rate $\sim \kappa[t]$, unlike the constant values in the $m = 0$ case. However, as we will demonstrate later in this supplemental material, for nearly all m values and for the majority of the relevant portion of the linear evolution, the amplitude of $Q_\pm[t]$ varies negligibly over time compared to its frequency or growth rate. As a result, the time evolution of $Q_\pm[t]$ is primarily governed by the imaginary part of $\kappa[t]$, denoted as $\text{Im}[\kappa[t]]$.

According to Eq. (S8a), $\kappa[t]$ retains the same form as $\kappa[0]$ (or $\kappa[t]$ in the $m = 0$ case), except that k is now replaced by the time-dependent term $k_{\text{eff}}[t] = k - mt$. In our numerical setup with $\mu = 1.5 \text{ cm}^{-1}$ and $\alpha = 1/3$, $\text{Im}[\kappa[0]] \neq 0$ for k within the range $(k_{\text{min}}, k_{\text{max}})$, where $k_{\text{min}} = \mu(1 + \alpha - 2\sqrt{\alpha}) \sim 0.3 \text{ cm}^{-1}$ and $k_{\text{max}} = \mu(1 + \alpha + 2\sqrt{\alpha}) \sim 3.6 \text{ cm}^{-1}$. The value of $\text{Im}[\kappa[0]]$ reaches a maximum of $\beta = 2\mu\sqrt{\alpha} \sim 1.73 \text{ cm}^{-1} \sim 58 \text{ ns}^{-1}$ at $k = k_0 = \mu(1 + \alpha) \sim 2 \text{ cm}^{-1}$, and symmetrically decreases on both sides of k_0 until it reaches zero. Importantly, β is constant over time. Eq. (S8a) also implies that replacing k with $k + mt$ leaves $\text{Im}[\kappa[t]]$ unchanged. This indicates that the value of $\text{Im}[\kappa[t]]$ for a given k at $t = 0$ appears at $k = k + mt$ at a later time t . As a result, the shape of $\text{Im}[\kappa[t]]$ in k -space remains unchanged over time, but $\text{Im}[\kappa[t]]$ shifts toward higher Fourier modes in the $k > 0$ (or $k < 0$) direction as time progresses, depending on whether $m > 0$ (or $m < 0$). The shift rate of the instability map ($\text{Im}[\kappa[t]]$ vs. k curve) can be well approximated by the shift rate of the fastest-growing Fourier mode at $k = k_0 \sim 2 \text{ cm}^{-1}$, expressed as $r_s = m/(k_{\text{max}} - k_0) \sim 19(m/\text{cm}^{-2}) \text{ ns}^{-1}$.

For a dense neutrino system whose linear growth in flavor space is predominantly governed by the maximum growth rate $\beta = 1.73 \text{ cm}^{-1} \sim 58 \text{ ns}^{-1}$, if the condition $\beta > r_s$, or equivalently $\gamma = \beta/r_s > 1$, is met, unstable Fourier modes with growth rates near the maximum β have enough time to grow independently, triggering flavor instability and nonlinear flavor conversion. This condition is satisfied for the small m ($\infty > \gamma \gtrsim O(100)$) and intermediate m ($O(100) > \gamma > 1$) values as discussed in the main text. Consequently, for both small and intermediate m , a dense neutrino gas initially in an unstable state, characterized by ELN crossings, will inevitably undergo fast flavor conversion. However, if r_s is greater than β (i.e., $\gamma = \beta/r_s < 1$), the instability map shifts too quickly, leaving insufficient time for unstable modes to grow, thus preventing the system from exhibiting significant fast flavor conversion. This situation arises for high m values ($m > 3$), indicating that even if the system is initially unstable, significant spatial inhomogeneity in the matter potential will render it completely stable, with no significant flavor growth. The critical value of m at which this occurs is given by $\gamma_{\text{crit}} = 1$, corresponding to $m_{\text{crit}} = 3 \text{ cm}^{-2}$. This analytical estimate for m_{crit} is in good agreement with the numerical solution, as clearly demonstrated by the time evolution of $S_\pm^{\text{trans}}[t]$, shown in Fig. 1 of the main text.

Using the stability analysis theory developed above, we now explore the linear behavior of the Fourier modes in detail for three distinct m regimes, examining each case individually. Additionally, we will compare our theoretical understanding with the full numerical solution of Eqs. (1a)-(1b) in the main text.

Small m regime

Eq. (S8a) can be rewritten as,

$$\kappa[t] = \kappa[0] \sqrt{1 + \frac{2mt((1+\alpha)\mu - k)}{\kappa[0]^2} + \frac{m^2 t^2}{\kappa[0]^2}}. \quad (\text{S15})$$

In our numerical simulation with parameters ($\mu = 1.5$, $\alpha = 1/3$) without the matter term, the unstable modes with significant growth rates contributing to the linear growth of flavor instability satisfy $\text{Im}[\kappa[0]] \sim O(\mu)$ and $k \sim O(\mu)$. For small m , with $mt \ll O(\mu)$ in the linear regime ($t \sim 0 - 0.5$ ns), $O(mt/\mu)$ and higher-order corrections in Eqs. (S8a)-(S8d) and Eq. (S11a) can be neglected to obtain a leading-order estimate for $\kappa[t]$, $k_{\text{eff}}[t]$, $N_1[t]$, $N_2[t]$ and $\det[P[t]]$ as,

$$\kappa[t] \sim \kappa[0] \sim i O(\mu), \quad (\text{S16a})$$

$$k_{\text{eff}}[t] \sim k \sim O(\mu), \quad (\text{S16b})$$

$$N_1[t] \sim N_1[0] \sim O(1), \quad (\text{S16c})$$

$$N_2[t] \sim N_2[0] \sim O(1), \quad (\text{S16d})$$

$$\det[P[t]] \sim \frac{-\kappa[0]}{\mu N_1[0] N_2[0]}. \quad (\text{S16e})$$

In Eq. (S16e), μ , $N_1[0]$, $N_2[0]$ are finite, while $\kappa[0] \neq 0$ for unstable k modes, ensuring $\det[P[t]] \neq 0$ and the existence of $P^{-1}[t]$ for small m cases throughout the linear regime. Eqs. (S16a)-(S16e) provide a leading-order estimate for the magnitude of each matrix element in $P^{-1}[t] \frac{dP}{dt}$ as well as the magnitude of $-iX_{1,2}[t]$ as,

$$\left| P^{-1}[t] \frac{dP[t]}{dt} \right| \sim \begin{pmatrix} O(\frac{m\alpha}{\mu}) & O(\frac{m\alpha}{\mu}) \\ O(\frac{m\alpha^2}{\mu}) & O(\frac{m\alpha^2}{\mu}) \end{pmatrix}, \quad (\text{S17a})$$

$$|-iX_{1,2}[t]| \sim O(\mu). \quad (\text{S17b})$$

With $\alpha < 1$ and small m , $O(m\alpha/\mu) \ll O(\mu)$ and $O(m\alpha^2/\mu) \ll O(\mu)$, Eqs. (S17a)-(S17b) show that all elements of $P^{-1}[t] \frac{dP[t]}{dt}$ can be neglected compared to $-iX_{1,2}$ in Eq. (S9), yielding the solution for $Q_{\pm}[k, t]$ as in Eqs. (S13a)-(S13b). Notably, to leading order, $\int_0^t \kappa[t] dt \sim \kappa[0]t$, and for initially unstable k modes, $\kappa[0]$ is complex. Eqs. (S16a)-(S16e) and Eqs. (S17a)-(S17b) provide an approximate solution for $Q_{\pm}[t]$ for the initially unstable k modes with small m , derived from Eqs. (S13a)-(S13b), as follows:

$$Q_+[t] \sim Q_+[0] e^{-i\mu(1-\alpha)t - i\kappa[0]t}, \quad (\text{S18a})$$

$$Q_-[t] \sim Q_-[0] e^{-i\mu(1-\alpha)t - i\kappa[0]t}. \quad (\text{S18b})$$

Eqs. (S18a)-(S18b) show that the leading order estimate for Q_{\pm} in small m cases matches that without the matter potential. The leading-order $\kappa[t] \sim \kappa[0]$ remains constant, indicating the instability map is almost time-independent ($\gamma \gg 1$), allowing Q_{\pm} for unstable k modes to grow independently at a fixed rate equivalent to the complex part of $\kappa[0]$ until nonlinear effects trigger fast flavor depolarization. The numerical solution for $|Q_+|$ in the unstable k range ($k \sim 0.3 - 3.6 \text{ cm}^{-1}$) confirms independent growth of $|Q_+|$ across all the unstable modes for $t \sim 0 - 0.6$ ns. The analytical estimate from Eq. (S18a) closely matches the numerical solution for $Q_+[t]$, as shown in Fig. 2(a) of the main text.

Intermediate m regime

Eq. (S8a) suggests that for an initially unstable k mode whose $\text{Im}[\kappa[0]] > 0$, $\text{Im}[\kappa[t]]$ decreases and approaches zero when mt increases. When $mt \lesssim k$ at $t = t_c$ such that the right-hand side of Eq. (S8a) vanishes, $\det[P[t]] = 0$, leading to the divergence of $P^{-1}[t]$. Around $t \sim t_c$, $P^{-1}[t]$ can be large so that the condition $P^{-1}[t] \frac{dP[t]}{dt} \ll X_{1,2}[t]$ can be violated, too. After that, $\kappa[t]$ for the same k mode acquires a real, nonzero value that increases over time. In our numerical calculations with intermediate m values, such a cancellation can happen for the initially unstable k modes within the range $k \in (0.3, 3.6) \text{ cm}^{-1}$ at different times during the simulation time frame $0 \leq t \leq 0.9$ ns, which leads to

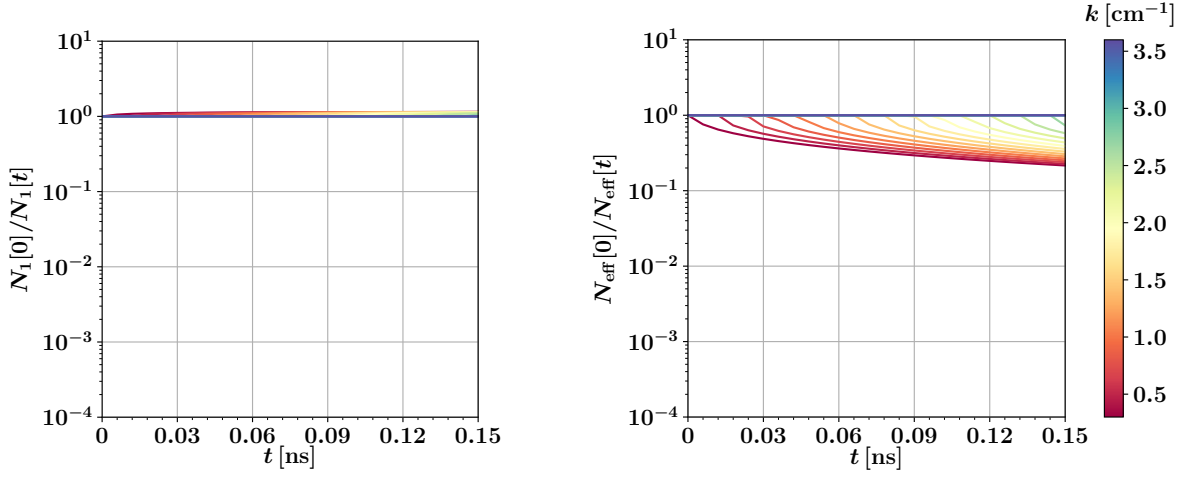


FIG. S1. : Time evolution of $N_1[0]/N_1[t]$ (left panel) and $N_{\text{eff}}[0]/N_{\text{eff}}[t]$ (right panel) for all initially unstable k modes ($k \in (0.3 - 3.6) \text{ cm}^{-1}$), with colors indicated by the color bar. Both quantities remain near $O(1)$ with minimal variation over $t \sim (0 - 0.15)$ ns.

qualitatively very different behavior than the small m limit as shown in Figs. 1 and 2 in the main text. Nevertheless, we find that the independent evolution equations Eq. (S13a)-(S13b) can still be used to approximate the system's evolution up to $t \lesssim 0.15$ ns, which will be discussed below.

The numerical solution for $|Q_+[t]|$ with $k \in (0.3, 3.6) \text{ cm}^{-1}$ and $m = 0.5 \text{ cm}^{-2}$ presented in Fig. 2 (middle panel) of the main text indicates that the linear evolution of the Fourier modes split into two groups when $t \lesssim 0.15$ ns: (i) for $k_{\min} \leq k < k_0$ ($k_{\min} = 0.3 \text{ cm}^{-1}$, $k_0 = 2 \text{ cm}^{-1}$), which remains stable, and (ii) for $k_0 \leq k \leq k_{\max}$ ($k_{\max} = 3.6 \text{ cm}^{-1}$), which evolves with similar growth rates. If we naively ignore the term $P^{-1}[t] \frac{dP[t]}{dt}$ (relative to $X_{1,2}[t]$) for all k modes, the linear evolution of $Q_{\pm}[t]$ can be derived by solving Eq. (S13a)-(S13b). Given that $N_1[t]$ and $N_{\text{eff}}[t]$ varies relatively little in time for $t < 0.15$ ns as shown in Fig. S1, one can approximately neglect the prefactors in front of the exponentials in Eqs. (S13a)-(S13b), which results in

$$Q_{\pm}[t] \sim Q_{\pm}[0] e^{-i\mu(1-\alpha)t \mp i \int_0^t \kappa[t] dt}. \quad (\text{S19})$$

Eq. (S19) suggests that the growth of $|Q_{\pm}[t]|$ is primarily influenced by the imaginary part of $\int_0^t \kappa[t] dt$, which for $m \neq 0$ can be expressed as:

$$\text{Im} \left[\int_0^t \kappa[t] dt \right] = \frac{4\alpha\mu^2}{2m} (K[t] + \theta[t]), \quad (\text{S20})$$

where

$$K[t] = \frac{(-k_{\text{eff}}[t] + \mu(1 + \alpha)) \text{Im}[\kappa[t]]}{4\alpha\mu^2}, \quad (\text{S21a})$$

$$\theta[t] = \begin{cases} \tan^{-1} \left(\frac{\text{Im}[\kappa[t]]}{k_{\text{eff}}[t] - \mu(1 + \alpha)} \right), & \text{if } k_{\text{eff}}[t] - \mu(1 + \alpha) > 0, \\ \tan^{-1} \left(\frac{\text{Im}[\kappa[t]]}{k_{\text{eff}}[t] - \mu(1 + \alpha)} \right) + \pi & \text{if } k_{\text{eff}}[t] - \mu(1 + \alpha) < 0. \end{cases} \quad (\text{S21b})$$

Fig. S2 shows that $\theta[t]$ consistently dominates over $K[t]$ at all times for all shown k modes. This allows us to neglect $K[t]$ in Eq. (S20) and compactly express the evolution of $|Q_{\pm}[t]|$ in terms of the time-dependent rotation of the angle $\theta[t]$, as follows:

$$|Q_{\pm}[t]| \sim |Q_{\pm}[0]| e^{\frac{4\alpha\mu^2\theta[t]}{2m}}. \quad (\text{S22})$$

Fig. 2(b) in the main text shows that the evolution given by Eq. (S22) for $k = \{0.3, 0.5, 0.7, 0.9, 1.03, 3, 3.4, 3.6\} \text{ cm}^{-1}$ (dashed lines) that belong to two different groups mentioned above closely follow the numerical simulation outcome up to $t \sim 0.15$. The underlying reason why these two groups evolve differently can be understood by examining the time evolution of $\theta[t]$ as further detailed below.

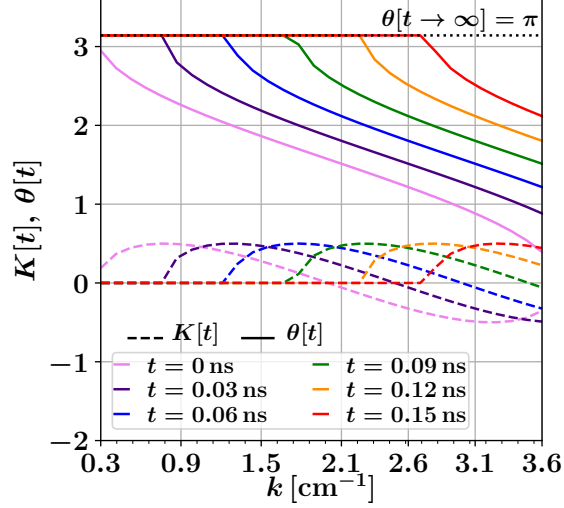


FIG. S2. : $K[t]$ and $\theta[t]$ as functions of k at different time snapshots ($t = (0, 0.03, 0.06, 0.09, 0.12, 0.15)$ ns) with colors indicated in the legend. Note that $K[t]$ and $\theta[t]$ are computed using Eqs. (S21a)-(S21b) with the parameter values used in our numerical simulation: $\mu = 1.5 \text{ cm}^{-1}$, $\alpha = 1/3$ and $m = 0.5 \text{ cm}^{-2}$. The black dotted curve represents $\theta[t]$ at $t \rightarrow \infty$, which equals π . $\theta[t]$ always dominates $K[t]$ over time and gradually approaches $\theta[t \rightarrow \infty] = \pi$ for all k , leading to the flattening of the $\theta[t]$ vs k curve.

Eq. (S22) suggests that the degree of the rotation or change of $\theta[t]$ is linked to the extent of flavor conversion or the growth of $|Q_{\pm}[t]|$. As t increases, $|k_{\text{eff}}[t] - \mu(1 + \alpha)|$ grows in magnitude for all k , with its sign becoming increasingly negative. While $\text{Im}[\kappa[t]] \geq 0$ for all k at all times, it gradually decreases over time across all k due to the shifting of the instability map in k space. This means that the angle $\theta[t]$ approaches a value near π as time progresses, regardless of k . Given $\mu = 1.5 \text{ cm}^{-1}$, $m = 0.5 \text{ cm}^{-2}$ and $\alpha = \frac{1}{3}$, at $t = 0$, we find $k_{\text{eff}}[0] - \mu(1 + \alpha) > 0$ for $k > 2 \text{ cm}^{-1}$ and $k_{\text{eff}}[0] - \mu(1 + \alpha) < 0$ for $k < 2 \text{ cm}^{-1}$. Therefore, for $k < 2 \text{ cm}^{-1}$ modes, $\theta[t]$ at $t = 0$ is already near but slightly less than π , as illustrated in Fig. S2. Consequently, as time progresses, the rotation or increase of $\theta[t]$ required to approach π is smaller for these modes. This reduced change in $\theta[t]$ leads to less growth for $k < 2 \text{ cm}^{-1}$ modes, explaining their relative stability. In contrast, for $k > 2 \text{ cm}^{-1}$ modes, $\theta[t]$ is much smaller than π , closer to 0, as shown in Fig. S2. As time progresses, $\theta[t]$ needs to undergo a much larger change or rotation to approach π . This significant rotation in $\theta[t]$ accounts for the unstable nature of $k > 2 \text{ cm}^{-1}$ modes. As described in Eq. (S21b), the tendency of $\theta[t]$ for all $k > 2 \text{ cm}^{-1}$ modes to increase over time and approach a k -independent value near π leads to the flattening of $\theta[t]$ across k -space, as shown in Fig. S2. According to Eq. (S22), this flattening in $\theta[t]$ over time causes $Q_{+}[t]$ for $k > 2 \text{ cm}^{-1}$ modes to grow at nearly the same rate as observed in Fig. 2(b) of the main text.

Now, let's examine the key assumption used in the above analysis behind Eqs. (S13a) and (S13b), and its consequence. As mentioned in the beginning of this subsection — the occurrence of $\det[P[t]] = 0$ at $t = t_c$ for the initially unstable k modes can happen at different times, which can invalid the condition $P^{-1}[t] \frac{dP[t]}{dt} \ll X_{1,2}[t]$. From Eq. (S6a)-(S6b), it is evident that the validity of this approximation depends on the time-dependent part of $X_{1,2}[t]$, which corresponds to $\pm\kappa[t]$, since the constant term $\mu(1 - \alpha)$ can be removed through a common rotation of $Q_{\pm}[t]$ as $Q_{\pm}[t] \rightarrow Q_{\pm}[t]e^{-i\mu(1-\alpha)t}$, preserving the length of $Q_{\pm}[t]$. Thus, we compute the ratio $R^{ij}[t] = \left| \frac{[P^{-1}[t] \frac{dP[t]}{dt}]^{ij}}{\kappa[t]} \right|$ over time up to $t = 0.15$ ns for $k = \{0.5, 1.0, 1.5, 3.0, 3.2, 3.4\} \text{ cm}^{-1}$ and show their values in Fig. S3. Here, $[P^{-1}[t] \frac{dP[t]}{dt}]^{ij}$ represents the (i, j) -th element of the matrix $P^{-1}[t] \frac{dP[t]}{dt}$, with $i, j = 1, 2$.

Fig. S3 shows that for $k > k_0$ modes, which undergo exponential growth at $t \leq 0.15$ ns, $R^{ij}[t]$ (for all $i, j = 1, 2$) consistently remains around $O(0.1)$ as $t_c > 0.15$ ns for these modes. Thus, their evolution up to $t \leq 0.15$ ns can be approximated by the solution of Eqs. (S13a) and (S13b) discussed above. However, for $k < k_0$ modes, Fig. S3 shows that their R^{ij} blows up at $t = t_c$ before $t = 0.15$ ns, roughly at where $mt \sim k$, which should have invalidated the assumption behind Eqs. (S13a) and (S13b). In principle, around $t = t_c$, the transformation in Eq. (S2) becomes invalid, and one should use

$$S_{\pm}^{\perp}[z, t] = \int_{-\infty}^{\infty} dk e^{ikz} Q_{\pm}[k, t]. \quad (\text{S23})$$

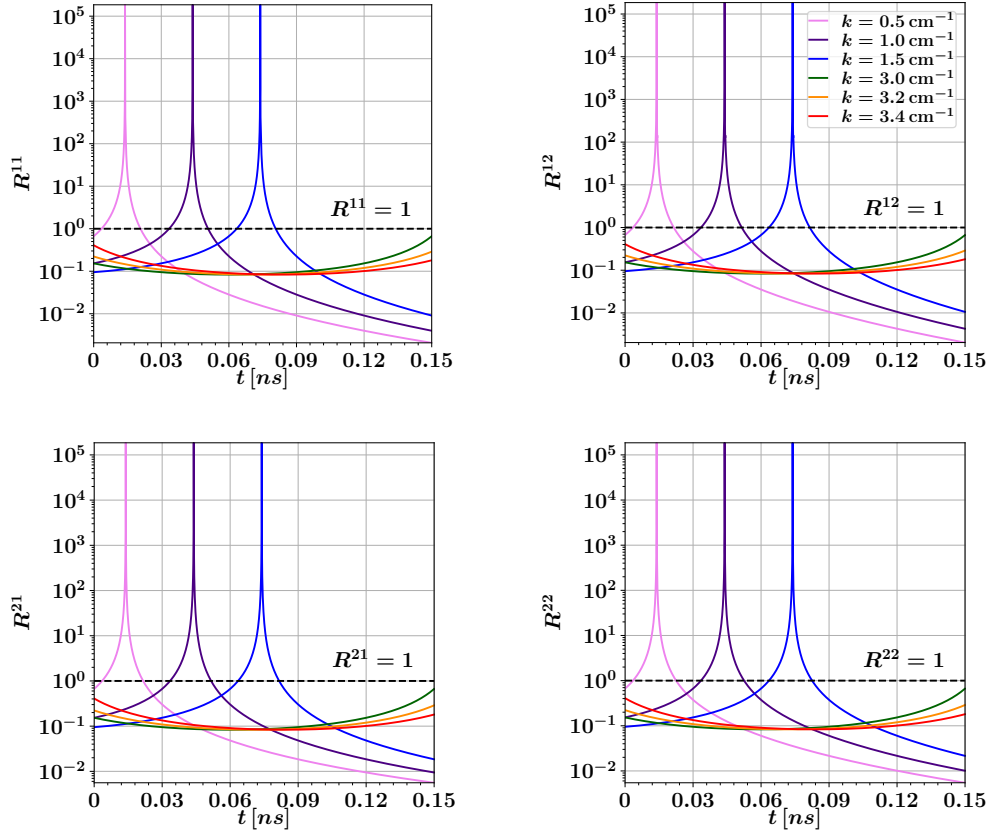


FIG. S3. : Time evolution of R^{11} , R^{12} , R^{21} and R^{22} shown in the top left, top right, bottom left, and bottom right panels, respectively, up to $t = 0.15$ ns for $k = \{0.5, 1, 1.5, 3, 3.2, 3.4\} \text{ cm}^{-1}$. Different colors in each plot represent R^{ij} values for various k modes, as indicated in the legend.

Using Eq. (S23) and Eq. (S1), the time evolution of $Q_{\pm}[k, t]$ can be written as [66],

$$\partial_t \begin{pmatrix} Q_+ \\ Q_- \end{pmatrix} = \begin{pmatrix} -ik + 2i\mu\alpha - i\Lambda_+[k, t] & -2i\mu\alpha \\ 2i\mu & ik - 2i\mu - i\Lambda_-[k, t] \end{pmatrix} \begin{pmatrix} Q_+ \\ Q_- \end{pmatrix}. \quad (\text{S24})$$

In Eq. (S24), $\Lambda_{\pm}[k, t]$ is defined as [66],

$$\Lambda_{\pm}[k, t] = \int_{-\infty}^{\infty} dk' \lambda[k'] Q_{\pm}[k - k', t], \quad (\text{S25})$$

where $\lambda[k]$ represents the Fourier transform of $\lambda[z]$ over the spatial domain $z \in (-\frac{\Delta z}{2}, \frac{\Delta z}{2})$. The transformation in Eq. (S23) fails to eliminate the explicit z dependence introduced by the $\lambda[z]$ term from Eq. (S1). As a result, an additional term, $\Lambda_{\pm}[k, t]$ must be included in Eq. (S24) to account for the coupling between Fourier modes caused by the inhomogeneous matter term. This means that mode-mode coupling due to matter inhomogeneity becomes important at $t \sim t_c$ (or when $mt \sim k$).

For the linear $\lambda[z]$ profile considered in this work $\lambda[z] = m(z + 30)$, $\lambda[k]$ can be expressed as,

$$\lambda[k] = \left(30m\Delta z - i\frac{m\Delta z}{k} \right) \frac{\sin \frac{k\Delta z}{2}}{\frac{k\Delta z}{2}} + i\frac{m\Delta z^2}{2} \frac{\cos \frac{k\Delta z}{2}}{\frac{k\Delta z}{2}}. \quad (\text{S26})$$

In the limit $\Delta z \gg 1$, the sinc functions in Eq. (S26) ($\frac{\sin \frac{k\Delta z}{2}}{\frac{k\Delta z}{2}}$ or $\frac{\cos \frac{k\Delta z}{2}}{\frac{k\Delta z}{2}}$) peak sharply at $k = 0$ and decay rapidly with increasing $|k|$. This ensures that the coupling term $\Lambda_{\pm}[k, t]$ for a specific mode $k = k_s$ only receives dominant contributions from modes near $k = k_s$, meaning $\Lambda_{\pm}[k_s, t] \sim \lambda[0]Q_{\pm}[k_s, t]$, with only minor contributions from other Fourier modes. In other words, the linear spatial variation of $\lambda[z]$ effectively localizes the coupling between Fourier modes, restricting it to interactions only between the neighboring modes. Since all $k < k_0$ modes are initially stable

at $t < t_c$ and the restriction of nearby mode coupling at $t \sim t_c$ ensures that they do not couple to the unstable $k > k_0$ modes, even if $P^{-1}[t] \frac{dP[t]}{dt} \gg X_{1,2}[t]$ around $t \sim t_c$, the continuity of $Q_{\pm}[t]$ guarantees that $Q_{\pm}[t]$ does not experience any significant discontinuous changes caused by the large values of $P^{-1}[t] \frac{dP[t]}{dt}$ that briefly appear at $t \sim t_c$. Consequently, these modes remain stable as predicted with Eqs. (S13a) and (S13b) that assume $P^{-1}[t] \frac{dP[t]}{dt} \ll X_{1,2}[t]$ at all times for $t < 0.15$ ns.

For $t > 0.15$ ns, $k - mt \sim 0$ happens also for unstable $k > k_0$ modes. This implies that mode-mode coupling effect kicks in and affects the growth behavior of these unstable modes. A detailed derivation of how they evolve requires solving Eq. (S24) with the mode-mode coupling term ($\lambda[k]$ in Eq. (S26)), which is beyond the scope of this work. Nevertheless, we highlight some features of the behavior of the Fourier modes beyond $t = 0.15$ ns based on the results from the numerical simulation and the nature of mode-mode coupling.

From Fig. S2, it can be observed that by $t \sim O(0.15)$ ns, $\theta[t]$ roughly stabilizes near π , becoming constant for $k < 3.6 \text{ cm}^{-1}$. According to Eq. (S22), this suggests that Q_+ should also remain constant after $t \sim O(0.15)$ ns. However, numerical results show that for $t > O(0.15)$ ns, $Q_+[t]$ for $2 \text{ cm}^{-1} < k < 3.6 \text{ cm}^{-1}$ modes continues to grow at a *synchronized* rate, hinting that this growth is carried by the mode coupling effect from modes of $k > 3.6 \text{ cm}^{-1}$ that were initially stable but now become unstable. Interestingly, for $k < 2 \text{ cm}^{-1}$ modes that are previously stable, they also start growing along with the unstable modes with larger k once the $|Q_{\pm}[t]|$ of all these synchronized modes become comparable to the $|Q_{\pm}[t]|$ of the initially stable modes, shown by Fig. 2(b) in the main text. We speculate that this effect is, once again, due to the mode-mode coupling—as the coupling term originates from Eq. (S25) which is proportional to $Q_{\pm}[t]$ of nearby modes, the mode coupling effect only becomes important when $|Q_{\pm}[t]|$ of neighboring modes are comparable.

This intriguing behavior of synchronization warrant a detailed exploration of the solution of Eq. (S24) in the linear regime as well as further detailed investigation on the impact of the quasistationary state of the system at the nonlinear regime, which we leave for future work.

Large m regime

When taking large m values, we can focus on the regime where $|mt| \gg |k|$ and $|mt| \gg \mu$ holds for unstable Fourier modes, implying a non-zero $\kappa[t]$ or the presence of $P^{-1}[t]$ at relevant times. This allows us to express $\kappa[t]$, $k_{\text{eff}}[t]$, $N_1[t]$, $N_2[t]$ in Eq. (S8a)-(S8d) as a series expansion in powers of $O(x)$ with $x \equiv \mu/(mt) \ll 1$, providing a leading-order magnitude estimate for $\left| P^{-1}[t] \frac{dP[t]}{dt} \right|$ and $| -iX_{1,2}[t] |$ as follows :

$$\left| P^{-1}[t] \frac{dP[t]}{dt} \right| \sim \begin{pmatrix} O\left(\frac{x^3\alpha}{t}\right) & O\left(\frac{x^2\alpha^3}{t}\right) \\ O\left(\frac{x^2\alpha}{t}\right) & O\left(\frac{x\alpha}{t}\right) \end{pmatrix} \delta_{[\text{Im}[\kappa[t]],0]} + \begin{pmatrix} O\left(\frac{x^2\alpha}{(1+\alpha)t}\right) & O\left(\frac{\alpha}{(1+\alpha)t}\right) \\ O\left(\frac{x^2\alpha}{(1+\alpha)t}\right) & O\left(\frac{\alpha}{(1+\alpha)t}\right) \end{pmatrix} (1 - \delta_{[\text{Im}[\kappa[t]],0]}), \quad (\text{S27a})$$

$$| -iX_{1,2}[t] | \sim O\left(\frac{\mu}{x}\right). \quad (\text{S27b})$$

Eqs. (S27a)-(S27b) suggest that with sufficiently high m values where $x \ll 1$ and $|\alpha| < 1$, the terms $| -iX_{1,2}[t] |$ are significantly larger than $||P^{-1}[t] \frac{dP[t]}{dt} ||^{ij}$, for all $i, j = 1, 2$. This justifies neglecting all matrix elements of $P^{-1}[t] \frac{dP[t]}{dt}$ in comparison to $-iX_{1,2}[t]$ in Eq. (S9). Additionally, since $\kappa[t] \neq 0$ in this limit, mode-mode coupling is irrelevant, and $Q_{\pm}[k, t]$ for each Fourier mode evolves independently as described by Eqs. (S13a)-(S13b).

To quantify this approximation and identify the time range in which this approximation is valid, we refer to the numerical example demonstrated in Fig. 2(c) of the main text with $\mu = 1.5 \text{ cm}^{-1}$, $\alpha = 1/3$, and $m = 20 \text{ cm}^{-2}$. We focus on $t \gtrsim 0.15$ ns when $Q_{\pm}[t]$ of all k modes decay at a uniform rate. For $m = 20 \text{ cm}^{-2}$ and $t \geq 0.15$ ns, we find $x \leq 0.015$, $| -iX_{1,2}[t] | \geq O(100) \text{ cm}^{-1}$ and $\max[||P^{-1}[t] \frac{dP[t]}{dt} ||^{ij}] \leq O(0.05) \text{ cm}^{-1}$ (where “max[...]” represents the largest matrix element), suggesting the error of neglecting $||P^{-1}[t] \frac{dP[t]}{dt} ||^{ij}$ is smaller than $O(0.1)\%$, validating the use of Eqs. (S13a)-(S13b) to account for the evolution. Note that at very early times when $t \ll 0.15$ ns, x can be as large as $O(1)$ or even larger, suggesting that the solution for $Q_{\pm}[k, t]$ provided by Eq. (S13a)-(S13b) may not be valid. Also noted is that for this numerical example, $\gamma \sim 0.14$, and the shift rate $2m/\Delta k \sim 385 \text{ ns}^{-1}$ exceeds the maximum growth rate $\beta \sim 58 \text{ ns}^{-1}$.

As shown in Fig. 2(c) of the main text, for $t < O(0.15)$ ns, $|Q_+[k, t]|$ for some k modes in $k \in (0.3, 3.6) \text{ cm}^{-1}$ grow by a few orders of magnitude from its initial value at a rate similar to its initial growth rate at $t = 0$, as these Fourier modes are initially unstable. However, this initial growth phase is short-lived, preventing the system from reaching nonlinearity. Instead, starting around $t \sim O(0.15)$ ns, $|Q_+[k, t]|$ for all the initially unstable k modes stops

increasing and starts to decline rapidly. This can be understood by noting from Eq. (S20)-(S21b) that for $x \ll 1$, $\text{Im}[\int \kappa[t] dt] \sim \text{Im}[\kappa[t]]t$, leading Eq. (S13a) to predict $Q[t] \propto \frac{N_1[0]}{N_1[t]} \frac{N_{\text{eff}}[0]}{N_{\text{eff}}[t]} e^{\text{Im}[\kappa[t]]t}$. Due to the rapid shift of $\text{Im}[\kappa[t]]$ in k -space, $|Q_+[k, t]|$ for all initially unstable k modes begins to decrease at a rate approximately equal to the shift rate of $\text{Im}[\kappa[t]]$, given by $r_s \sim m/(k_{\text{max}} - k_0) \sim 385 \text{ ns}^{-1}$ for $m = 20 \text{ cm}^{-2}$. This behavior, shown by the black dashed curve in Fig. 2(c) of the main text, aligns well with numerical results. Note that for large m values, the rapid decline of $\text{Im}[\kappa[t]]$ results in a very short decay phase of $O(1/r_s) \sim O(0.1)$ ns, during which variations of $N_1[t]$ and $N_{\text{eff}}[t]$ are negligible, allowing them to be treated as constants, making $|Q_+[k, t]|$ primarily follow the time evolution of $\text{Im}[\kappa[t]]$. Thus, beginning at $t \sim 0.15$ ns and within approximately $O(10/r_s) \sim O(0.1)$ ns, $|Q_+[k, t]|$ for all the initially unstable k modes with $k \in (0.3, 3.6) \text{ cm}^{-1}$ stabilize. Thereafter, $|Q_+[k, t]|$ for these k modes remains stable over time, as evident in Fig. 2(c) of the main text. The long-term stability of $|Q_+[k, t]|$ for these k modes at later times follows from Eq. (S8a), as in the limit $x \ll 1$, we obtain $\kappa[t] \sim mt$, leading to $\text{Im}[\kappa[t]] \sim 0$, $N_1[t] \sim 1$, $N_{\text{eff}}[t] \sim mt$. This shows that the dense neutrino gas, initially unstable to fast oscillations, can behave as a stable system in the presence of matter potential with large spatial variation – a general result independent of the choice of the space-time domain in our numerical simulation.